

MASS AND MAGNETIC DISTRIBUTIONS IN SELF GRAVITATING SUPER ALFVÉNIC TURBULENCE WITH AMR.

DAVID C. COLLINS¹, PAOLO PADOAN², MICHAEL L. NORMAN¹, HAO XU³*Draft version August 23, 2010*

ABSTRACT

In this work, we present the mass and magnetic distributions found in a recent Adaptive Mesh Refinement (AMR) MHD simulation of supersonic, super-Alfvénic, self gravitating turbulence. Power law tails are found in both mass density and magnetic field probability density functions, with $P(\rho) \propto \rho^{-1.6}$ and $P(B) \propto B^{-2.7}$. A power law relationship is also found between magnetic field strength and density, with $B \propto \rho^{0.5}$, throughout the collapsing gas. The mass distribution of gravitationally bound cores is shown to be in excellent agreement with recent observation of prestellar cores. The mass to flux distribution of cores is also found to be in excellent agreement with recent Zeeman splitting measurements.

Subject headings: methods: numerical — AMR, MHD

1. INTRODUCTION

Understanding the details of star formation is one of the great open problems in astrophysics today. One of the central questions is the role of magnetic fields. Two opposite paradigms have been explored during the study of this problem. The earliest paradigm argues for strong fields that dominate the process (Shu et al. 1987; Mouschovias 1987a,b) and yield their dominance by way of ambipolar diffusion; the other extreme argues for relatively weak fields that at most alter the thickness of shocks (Padoan & Nordlund 1999; Padoan et al. 2007), with the majority of the details being determined by the turbulence.

Central to the development of the second paradigm has been the development of more advance computing hardware and software. Only a handful of simulations have been performed that incorporate all three necessary aspects: turbulence, gravity, and magnetic fields. Notably are Gammie et al. (2003), Li et al. (2004), Heitsch et al. (2001), Vázquez-Semadeni et al. (2005), Padoan & Nordlund (2009), Price & Bate (2008, 2010). The enormous range of scales at work in this problem have motivated the development of high dynamic range techniques, namely AMR (Fromang et al. 2006; Collins et al. 2010) and the addition of MHD to SPH (Price & Monaghan 2004). These techniques are beginning to yield interesting results on the nature of MHD in star formation (Price & Bate 2008; Dib et al. 2010).

In this work we focus on the distribution of mass and magnetic fields in super-Alfvénic simulation using high resolution AMR simulations. Section 2 will introduce the numerical algorithm and discuss the initial conditions and parameters of the simulation. In Sections 3 and 4 we present the volume and mass weighted density PDF for both density and magnetic field. In Section 5 we discuss the relation between mass density and magnetic

field strength. In Section 6, we discuss the relationship between line-of-sight magnetic field strength and column density (typically used as a proxy for the mass-to-flux ratio M/Φ , where M is the mass, and Φ is the magnetic flux), and compare to recent observations. In Section 7 we present the mass distribution of cores, and compare to observations of protostellar cores. In Section 8 we will conclude.

2. NUMERICAL MODEL

2.1. *Simulation software*

The simulation was performed with the MHD extension of Enzo by Collins et al. (2010). It employs the MHD Godunov solver of Li et al. (2008) to solve the MHD equations; to constrain $\nabla \cdot B$ it employs the CT scheme of Gardiner & Stone (2005); the AMR refinement is done with the divergence free interpolation of Balsara (2001). An isothermal equation of state and ideal MHD are assumed throughout.

Refinement is performed such that the Jeans length,

$$\lambda_J = \sqrt{\frac{\pi c_s^2}{G\rho}},$$

where c_s is the sound speed and G is the gravitational constant, is resolved by four grid zones everywhere. Thus, whenever the density in a zone is above the "True Density"

$$\rho_T = \frac{\pi^2 c_s^2}{16G\Delta x^2},$$

that zone is flagged for refinement. The maximum number of levels is 4. With a base grid of 128^3 , this gives a maximum effective resolution of 2048^3 .

2.2. *Simulation Parameters*

We began with a uniform density and magnetic field with no self gravity, and stirred with a Gaussian random field with no compressional modes, with power distributed in a top-hat between between $1 \leq k \leq 2$ and mean Mach number 8.9. Driving is done in the same manner as Mac Low (1999), such that the energy injection rate is constant. After a number of dynamical times,

¹ Center for Astrophysics & Space Sciences and Department of Physics, University of California at San Diego, La Jolla, CA

² ICREA-ICC, University of Barcelona, Spain

³ Theoretical division, Los Alamos National Lab, Los Alamos, NM

gravity was activated. This time is $t = 0$. Driving continued for the duration of the collapse.

The initial uniform fields have a ratio of gas to magnetic pressure of $\beta = 8\pi c^2 \langle \rho \rangle / \langle B^2 \rangle = 22.2$, but the mean squared field strength has been amplified by the driving so that when gravity is turned on at $t = 0$, $\beta = 0.2$. This yields an Alfvén Mach number of 2.8 at $t = 0$. have been chosen so that $\alpha = 5\sigma^2 R / (3GM) \approx 1$, where σ is the three dimensional velocity dispersion, M is the total mass in the box, and R is half the width of the box. The typical parameter used to measure the relative effects of magnetic and gravitational energy is the mass-to-flux ratio in units of the critical value for support. If we use the critical value for a sheet, as in Nakano & Nakamura (1978), $(M/\Phi)_c = (4\pi^2 G)^{-1/2}$, the uniform (pre-turbulence) cube gives us

$$\lambda = (M/\Phi)/(M/\Phi)_c = 18.7. \quad (1)$$

Mass to flux is a reasonable quantity to parameterize magnetic support for simple geometries, like spheres and disks. However, for situations like the one presented here, in both the turbulent box at $t = 0$ and the prestellar cores discussed later, the spatial structure of the objects in question are not easily defined. We find it more instructive to examine the ratio of energies. For sake of comparison to M/Φ , we define

$$\lambda_E = \sqrt{E_G/E_B}, \quad (2)$$

where

$$E_G = G \int \int \frac{\rho(r)\rho(r')}{|r - r'|} d^3r d^3r' \quad (3)$$

$$E_B = \int \frac{B^2}{8\pi} d^3r. \quad (4)$$

For the initial conditions at $t = 0$ (after the initial turbulent evolution, but before gravitational collapse), we have

$$\lambda_E = 6.5 \quad (5)$$

For reference, a sphere with critical mass $M_c = \Phi/(2\pi\sqrt{G})$, $\lambda_E = 0.2$.

In a similar vein, if we define $\alpha_E = 2E_K/E_G$ as the ratio of measured gravitational energy to total kinetic energy $E_K = \frac{1}{2} \int \rho v^2 d^3r$, we find for our data at $t = 0$

$$\alpha_E = 0.64. \quad (6)$$

2.3. Physical Scaling

Although these simulations are scale free, we use a box size of 10 pc and density of 300cm^{-3} for the analysis presented here. This gives a resolution on the finest zones of 1000 AU and a mean mass density $\rho_0 = 1.2 \times 10^{-21}$ g. The sound speed is set to be 0.2 km s^{-1} , giving a temperature of $\approx 10\text{ K}$. Mean and RMS magnetic fields are 0.6 and $2.7\text{ }\mu\text{G}$, respectively, with the mean along the \hat{z} direction. These units give a total mass of $1.2 \times 10^4 M_\odot$.

Rescaling can be found with the following relations:

$$t_{\text{ff}} = \sqrt{\frac{3\pi}{32G\rho}} \quad (7)$$

$$L \propto T^{1/2} \rho^{-1/2} \quad (8)$$

$$M \propto T^{3/2} \rho^{-1/2} \quad (9)$$

$$c_s \propto T^{1/2} \quad (10)$$

$$B \propto T^{1/2} \rho^{1/2}. \quad (11)$$

2.4. Core definition

We select cores with the algorithm described by Smith et al. (2009) which selects topologically connected density isosurfaces at a spacing of $\delta\rho = \rho_i/\rho_{i-1}$ that have no substructure; that is, a contour at ρ_{i-1} that contains zero or one contour above ρ_i . This is a similar definition to that used by Padoan et al. (2007) and Schmidt et al. (2010), both of whom reported no significant effects due to variations in $\delta\rho$, provided $\delta\rho < 1.16$. In our simulation, $\delta\rho = 1.12$. A core is determined to be bound if its gravitational energy is at least twice as large as the sum of kinetic, thermal, and magnetic energies. All analysis has been performed with the AMR analysis package *yt* (Turk 2008).

All analysis in this section takes place at a single snapshot, $t = 0.75t_{\text{ff}}$. At this time, there are 148 cores that match the definition of bound. Figure 1 shows a projection of density at this timestep in the left panel, and a close up of a portion of the column density map in the right panel with core boundaries drawn. All cores drawn are associated with topologically isolated, gravitationally bound objects, but some have their features washed out by projection effects.

3. DENSITY PDF

One of the most prominent consequences of supersonic turbulence is the log-normal distribution of densities (Vazquez-Semadeni 1994; Padoan et al. 1997a,b; Scalo et al. 1998; Passot & Vázquez-Semadeni 1998; Nordlund & Padoan 1999; Klessen 2000; Padoan & Nordlund 2002, 2009; Federrath et al. 2008b). This has been used to predict several properties of star formation, including the Initial Mass Function of stars (IMF) (Padoan & Nordlund 2002; Padoan et al. 2007), brown dwarf frequency (Padoan & Nordlund 2004) and the star formation rate (Krumholz & McKee 2005). Here we will discuss the PDFs one expects to see from isothermal turbulence, and what has been seen in our simulations with the inclusion of self gravity.

The central limit theorem states that the sum of a sufficiently large number of uncorrelated events will form a Normal, or Gaussian, distribution. A corollary of this is a sufficiently large number of random *multiplicative* events will form a lognormal distribution. This distribution has been experimentally verified in a large number of different simulations, both pure hydro (Vazquez-Semadeni 1994; Padoan et al. 1997b; Kritsuk et al. 2007, 2009) and MHD (Li et al. 2004; Lemaster & Stone 2008; Kritsuk et al. 2009).

The log-normal distribution is given by

$$P(x)d\ln x = \frac{1}{\sqrt{2\pi\sigma^2}} \exp\left[-\frac{(\ln x - \mu)^2}{2\sigma^2}\right] d\ln x \quad (12)$$

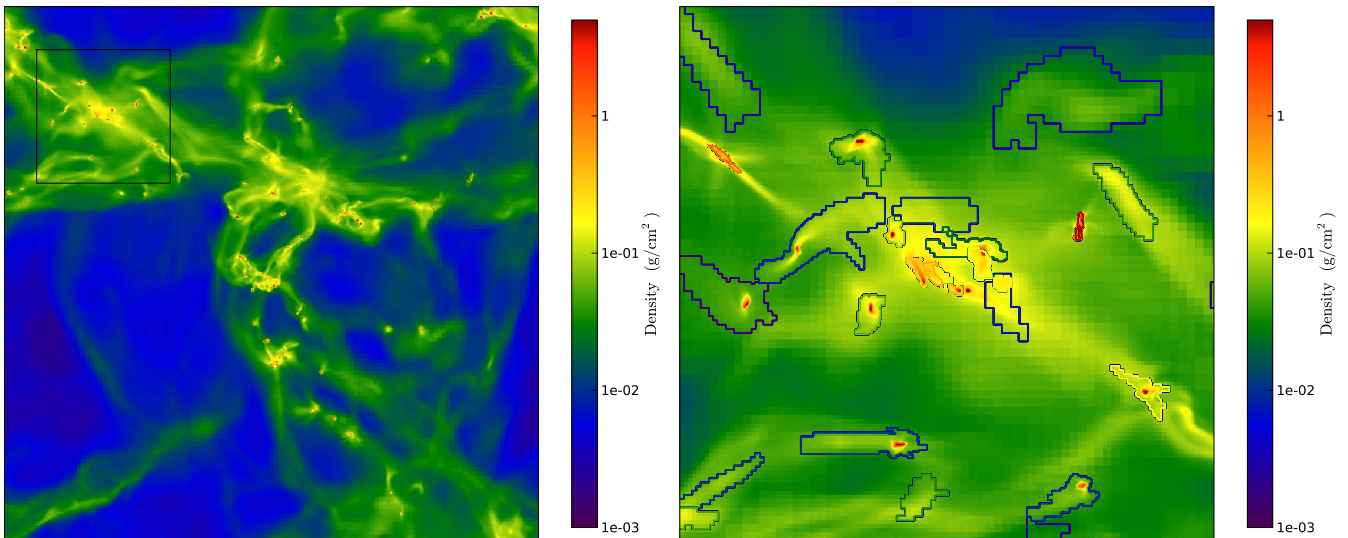


Figure 1. Projection of the full domain at $t = 0.75t_{ff}$ (left) and a close up of the squared region, including curves indicating the edges of all bound cores in the region (right).

where $x = \rho/\rho_0$ is the over density, and $\mu = -\sigma^2/2$ is the mean of $\ln x$. For pure hydrodynamical turbulence,

$$\sigma = \sqrt{\ln(1 + b^2 \mathcal{M}^2)} \quad (13)$$

where b has been determined numerically to lie between 0.3 and 0.4 (Padoan et al. 1997b; Federrath et al. 2008b; Kritsuk et al. 2007; Beetz et al. 2008; Kritsuk et al. 2010b; Federrath et al. 2010). The value b has been shown to vary by as much as a factor of 3, depending on the ratio of solenoidal to compressive forcing (Federrath et al. 2008b, 2010).

For driven MHD turbulence, Lemaster & Stone (2008) find that

$$\sigma_{\text{LM08}} = \sqrt{|-0.72 \ln[1 + 0.5\mathcal{M}^2] + 0.20|}, \quad (14)$$

and is insensitive to the magnetic field strength.

Figure 2 shows density PDF $P(\rho)$ for two snapshots: at $t = 0$ (left) and $t = 0.75t_{ff}$ (right). In both plots, the solid line is the measured PDF and the dashed line is the fit to a lognormal. Table 1 shows the fit parameters. The addition of self gravity causes the PDF to widen and the mean to decrease. We find that $b = 0.3$ for our initial conditions, similar to Kritsuk et al. (2007), but $b = 0.5$ for the collapsed snapshot; we also find that the dispersion, σ_{LM08} , found by Lemaster & Stone (2008) is in better agreement with the collapsed state of the simulation.

When turbulence simulations are performed in the presence of self gravity, several authors (Klessen 2000; Slyz et al. 2005; Vázquez-Semadeni et al. 2008; Federrath et al. 2008a; Kritsuk et al. 2010a) find that the log-normal PDF underestimates the high density tail of the measured PDF. Slyz et al. (2005) fit the high density tail to a power law with index of -1.5 . Klessen (2000) does not fit a power law, but the resolution of those simulations is much lower than what we present here. Vázquez-Semadeni et al. (2008) mention the existence of a power law, but say nothing further. Observationally, Kainulainen et al. (2009) found power law wings in column density distributions of active star forming regions, and a similar high density power law has been seen

Table 1
Fit parameters.

t/t_{ff}	\mathcal{M}	μ	σ	χ^2	b	σ_{LM08}
0	8.15	-0.80	1.35	4.6×10^{-6}	0.27	1.67
0.75	8.57	-1.86	1.74	1.6×10^{-6}	0.52	1.65

in Aquila (Philippe André, private communication.), Our work is the first reported case in an MHD simulation.

Kritsuk et al. (2010a) find an extended two part power law, with index -1.7 at intermediate densities, and -1 at high densities. They provide the first explanation of this power law, associating it with a self-similar singular isothermal sphere. In such a sphere, $\rho \propto r^{-2}$, thus $V(\rho) \propto \rho^{-3/2}$.

Figure 3 shows both volume-weighted PDF $P(\rho)$ and mass-weighted PDF $M(\rho)$, with the power law fits of -1.64 and -0.64 , respectively, in the range of $\rho = 10 - 1000$. The dashed line in Figure 3 is the same curve as the solid line in Figure 2, but here with the mid to high density power law emphasized. This power law breaks down above a density of 1000, likely due to resolution effects, as the maximum resolvable density in the simulation, according to the Truelove condition (Truelove et al. 1997), is a $\rho/\rho_0 = 1623$. The exponent we find is quite close to the -1.7 found by Kritsuk et al. (2010a), and in reasonable agreement with the -1.5 they predict from a singular isothermal sphere. Federrath et al. (2008a) also measure the density PDF from a driven, self-gravitating turbulence simulation (without magnetic fields) with a set of Lagrangian tracer particles. The tracer particles in their work also follow a power law tail, with an index of -0.6 ± 0.1 , (Federrath 2010, private communication) consistent with our mass-weighted $M(\rho)$.

4. MAGNETIC PDF

Figure 4 shows the volume-weighted PDF of the magnetic field at $t = 0$ in a semi-log plot. In agreement with Padoan & Nordlund (1999), we find a roughly exponential tail at high field strength. This intermittent distribution in the magnetic field is caused by the large field

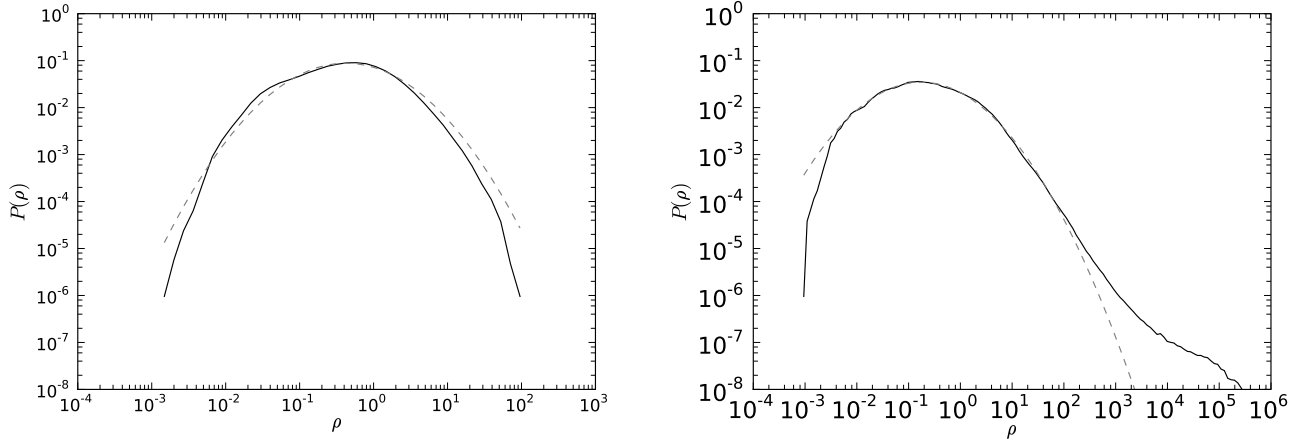


Figure 2. Density PDFs of the initial conditions (left) and after $t = 0.75t_{ff}$ (right). Both are fit to lognormal distributions (dashed lines).

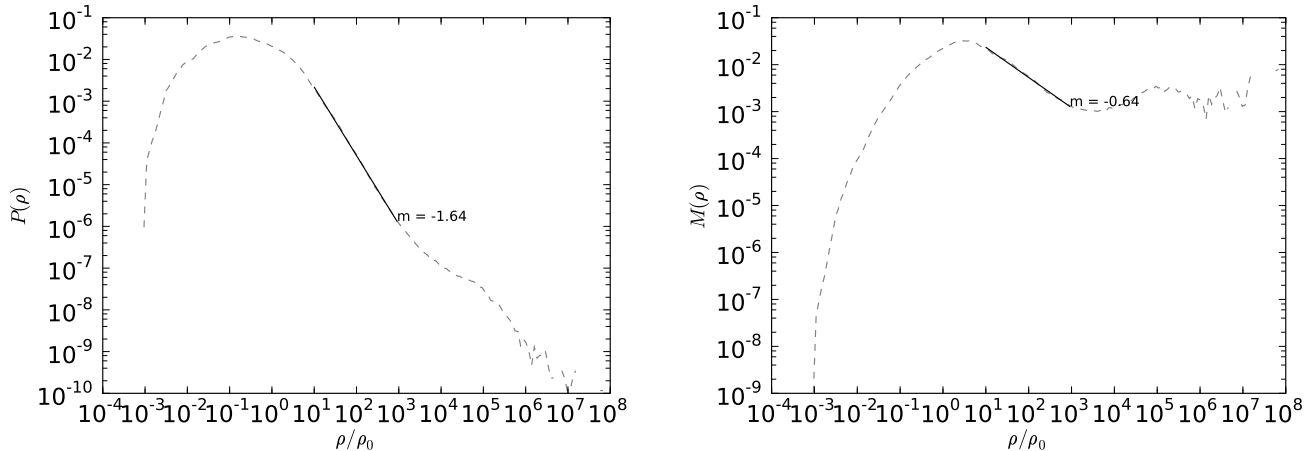


Figure 3. Volume (left) and mass (right) weighted density PDFs at $t = 0.75t_{ff}$, with power law fits.

amplifications by the strong, three dimensional compressions made possible by the large kinetic energy, relative to the magnetic energy, of the super-Alfvénic turbulence.

The left panel of Figure 5 shows the probability density function for the magnetic field strength, $P(B)$ for $t = 0$ (solid line) and $t = 0.75t_{ff}$ (dashed line), here in a log-log plot. The most significant aspect of this figure is the strong power law tail after the collapse has evolved. Gravitational collapse amplifies the peak magnetic field strength by 2 orders of magnitude (in fact a factor of 320), and creates a prominent power law tail. This powerlaw tail is fit by $P(B) \propto B^x$, with $x = -2.74$. If one naively takes $P(\rho) \propto \rho^{-1.5}$ as expected from a singular isothermal sphere (as in Section 3) and $\rho \propto B^2$ (as in other simulations (Li et al. 2004) and observations (Bertoldi & McKee 1992; Crutcher 1999) of dense cores), one arrives at $x = -3$, which is quite close to the value we find here. Details will be discussed in the next Section, where we measure the relationship between B and ρ in our simulation.

The right panel of Figure 5 shows the mass-weighted PDF, $M(B)$ for the same snapshots as the left panel. If we fit a power law to the same field strength range that was used for $P(B)$, we find $M(B) \propto B^m$, where $m = -0.4$. However, the power law in $M(B)$ is not nearly as well defined as for $P(B)$. This is due two related effects: the power law relation between ρ and B is less well defined at field strengths above $B = 100\mu\text{G}$ (see Figure 7 in the next section); and the power law in density breaks down above $\rho/\rho_0 > 1000$, likely due to resolution effects (see Figure 3).

5. FIELD STRENGTH VS. DENSITY

Figure 6 shows a contour plot of magnetic field strength vs density, colored by fraction of mass in each (B, ρ) bin. The left panel shows $t = 0$, before the action of gravity. As in Padoan & Nordlund (1999), the upper envelope is matched by a power law roughly of the form $B \propto \rho^{0.4}$, and the scatter is quite large in both B and ρ . The large scatter in field strength is due to

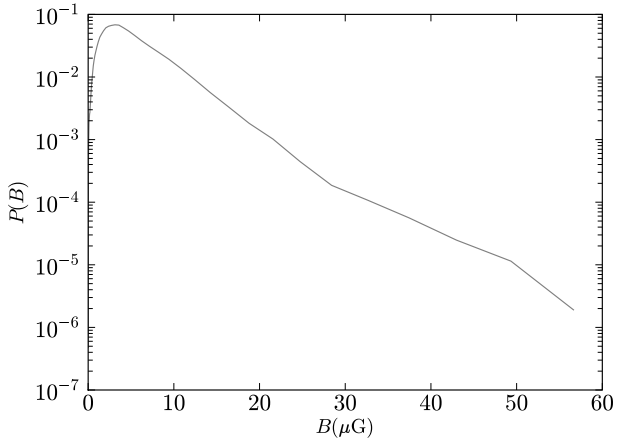


Figure 4. Semi-log plot of $P(B)$ at $t = 0$. A roughly exponential tail can be seen at high field strength, consistent with earlier super-Alfvénic turbulence simulations.

the fact that only the component of the field perpendicular to a shock is amplified, but due to the weak nature of the magnetic field, the relative orientations of \vec{B} and the shock are not correlated. Padoan & Nordlund (1999) demonstrated that in models with larger magnetic field strength (sub-Alfvénic turbulence), the flow is constrained to move primarily along the field lines, significantly decreasing the field strength amplification power of the turbulence, and decreasing the scatter in the magnetic field strength. The right panel in Figure 6 shows the $B - \rho$ relation at $t = 0.75t_{ff}$, after gravity has taken effect. Several features are noticeable. Both B and ρ are amplified by almost four orders of magnitude by the gravity, and the initial scatter in the distribution remains imprinted on the self gravitating distribution. The relation gets more shallow at $\rho/\rho_0 > 10^3$, which is the same density at which the power law slope seen in $P(\rho)$ changes. As before, this is likely due to resolution effects. Another feature of figure 6 is that the upper envelope slope increase sharply at $\rho/\rho_0 > 5$. Above this density, gravitational collapse has overtaken the dynamics, as evidenced by the onset of the power law in the density PDF. As these motions are three dimensional contractions, rather than the one dimensional compression due to shocks, the amplification is stronger than what is possible from the turbulence alone.

Figure 7 shows a mass weighted average B as a function of density bin, which has been fit to a power law between over densities of 10 and 1000. We find $B \propto \rho^{0.48}$. This behavior has been predicted or observed by several other authors: Fiedler & Mouschovias (1993) predicted $B \propto \rho^\kappa$, with $\kappa = 0.44 - 0.5$, though this was done in a quasi-static collapse model with ambipolar diffusion; both Bertoldi & McKee (1992) and Crutcher (1999) found a similar result in dense molecular cores and interpreted it as constancy of the Alfvén speed; Li et al. (2004) found this behavior for central density and magnetic field strengths. Figure 6 demonstrates that this behavior is endemic to the entire collapse process, not just the high density collapsed objects.

6. MASS TO FLUX RATIO

Figure 8 shows line-of-sight magnetic field strength, B_{los} , vs column density, N , for three populations of cores: CN Zeeman splitting measurements of Falgarone et al. (2008); OH Zeeman splitting measurements of Troland & Crutcher (2008); and bound objects in our simulation. Color shows $\lambda_E = \sqrt{E_G/E_B}$, our adopted proxy for mass to flux ratio. The left plot shows $t = 0$, the right plot shows $t = 0.75t_{ff}$. In the simulated points, the line of sight is taken along each of the three coordinate axes, so that there are three points in the plot for each simulated core; B_{los} is the density weighted average of each field quantity, and $N = M/A$, the total computed mass of the core divided by the area projected along that axis. The observational points are currently the best data available to relate magnetic field strength to mass, and some of the only magnetic field measurements for high density protostellar cores. The ratio between these quantities is often used as a proxy for mass-to-flux ratio λ as

$$\lambda = c_g \frac{N(H_2)}{B_{los}} \frac{\sqrt{G}}{c_\Phi}, \quad (15)$$

where $c_g = (1/2, 1/3)$ is a geometrical correction for (spherical, sheet) projection effects, and $c_\Phi = (0.12, 1/2\pi)$ is a correction found numerically for equilibrium configurations of a (sphere, sheet), respectively (Bourke et al. 2001). Here, we directly compare B_{los} and $N(H_2)$. This allows us to eliminate the need for either correction factor and compare the results of our model directly to the observations.

We find that our cores and the observed cores have almost the same distribution in the $B_{los}-N$ space. This shows that the early evolution of prestellar cores is well reproduced with isothermal super Alfvénic turbulence and self-gravity. Simulations without self gravity by Lunttila et al. (2008) successfully reproduce the lower density OH measurements, but lack the density range to reproduce the CN observations. This is also seen in the left panel of Figure 8, which shows the initial time $t = 0$, at which only the effects of turbulence are felt by the gas. The inclusion of self gravity and the large range of density scales allowed by AMR reproduces the higher density CN points.

The color of the simulated points corresponds to $\lambda_E = \sqrt{E_G/E_B}$, non-spherical analog of $\lambda = (M/\Phi)/(M/\Phi)_c$. Li et al. (2004) found that $\lambda > 10$ for all cores in question. We find that $\lambda_E > 1$ for all objects, which, using the spherical case as a guide, is analogous to $\lambda > 5$, so our results are in reasonable agreement with theirs.

The simulated points at $t = 0.75t_{ff}$ in figure 8 are best fit by a power law

$$B_{los} = N^{0.57} \quad (16)$$

Collapse that preserves mass-to-flux would have an exponent of 1, by equation 15. Since ideal MHD preserves M/Φ along a flux tube, this indicates that flow along the field lines must be responsible for some of the dynamics. As discussed by Padoan & Nordlund (1999), this is due predominantly to flow along the magnetic field lines. This flow is due predominantly to kinematic alignment between the velocity and magnetic field, wherein the kinetic energy stretches the magnetic field, hence aligning the two. The relationship in equation 16 is also expected

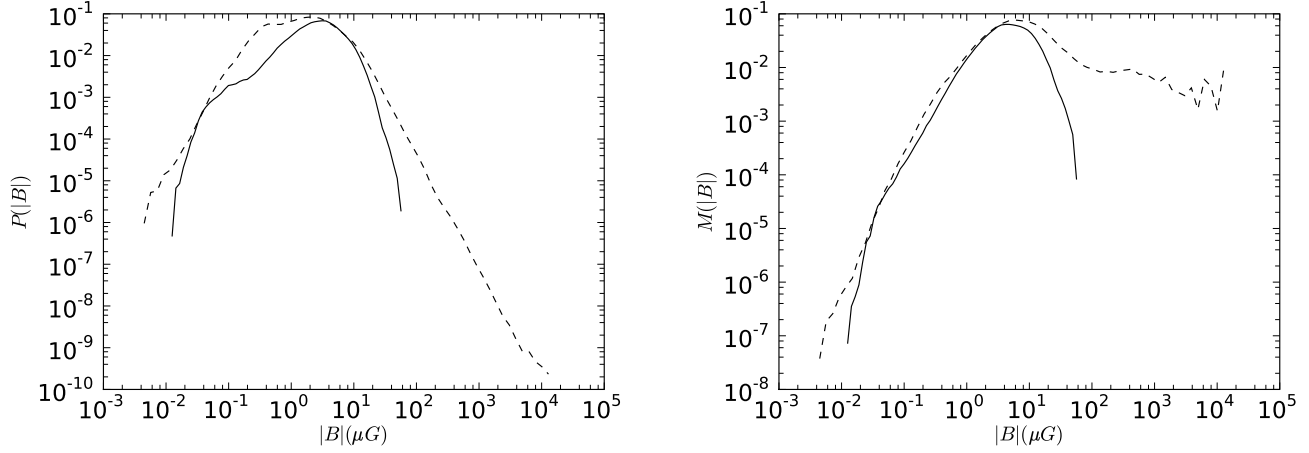


Figure 5. Magnetic field PDF $P(|B|)$ (left) and mass-weighted PDF $M(|B|)$ (right) for $t = 0$ (solid line) and $t = 0.75t_{ff}$ (dashed line).

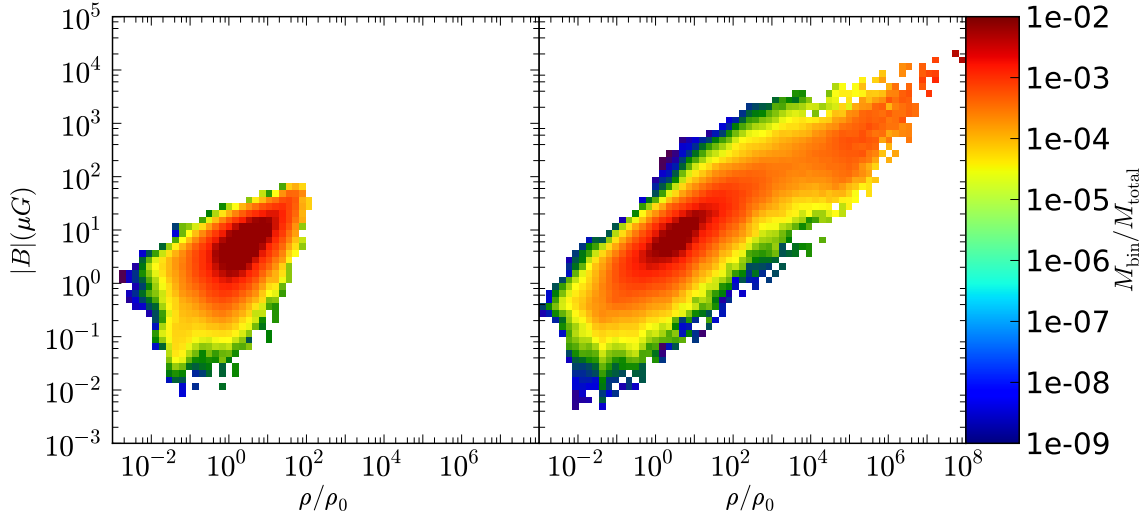


Figure 6. Magnetic field strength vs. density for all zones in the simulation for $t = 0$ (left) and $t = 0.75t_{ff}$ (right). Color field shows total mass fraction in each (B, ρ) bin.

from figure 6, demonstrating that the local properties of the core are dictated by the global flow properties.

7. CORE MASS FUNCTION

One of the open questions in star formation is the origin of the stellar initial mass function (IMF). Salpeter (1955) first measured this and fit it to a power law,

$$dN = 0.03 \left(\frac{M}{M_{\odot}} \right)^{\alpha} dM. \quad (17)$$

$$\alpha = -2.35 \quad (18)$$

This fit was done between 1 and $10 M_{\odot}$. The exact value of the exponent in the 1 to $10 M_{\odot}$ range is still under investigation (Scalo 2005), though recent measurements give the range of α to be between -2.3 and -2.8.

It has been proposed that the IMF and CMF are directly related to one another, either directly (Motte et al.

1998) or with some fraction of each core lost in the final collapse and accretion phase (Enoch et al. 2008). This implies that the IMF is determined by the global or large scale processes of star formation, in our model the combined effects of turbulence and gravity, as in the model of Padoan & Nordlund (2002). Alternative models have the IMF set by local physics, once protostars have formed within the prestellar condensations. These models include the competitive accretion model of Bonnell et al. (2001), wherein the population of neighboring protostars influences the final mass of any given star; and models of Shu et al. (1987) or Myers (2010), where protostellar outflows halt or slow the inflow of gas onto the protostar.

Figure 9 shows the mass distribution for all bound cores. The fit to the high end of the distribution is $n(M) \propto M^{-2.1 \pm 0.6}$. The fit was performed by fitting a power law between the peak and the highest bin for

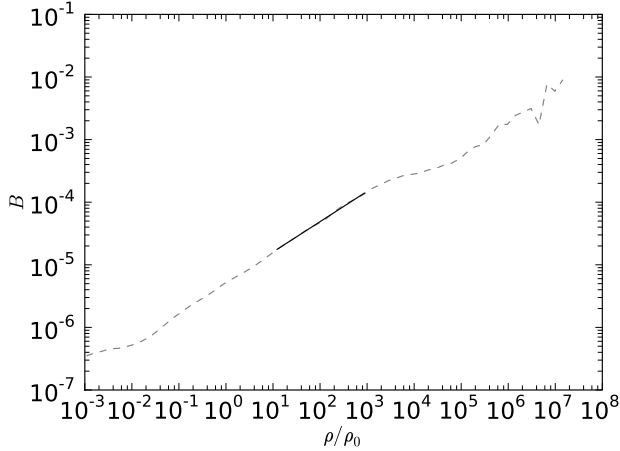


Figure 7. Mass weighted average B vs. ρ (dotted line) and fit to the range where the density PDF is also a clear power law (solid line). The fit is a power law with exponent 0.48.

a succession of bins between 5 and 25. We find good agreement between our slope and the IMF slopes mentioned above, and the slope of -2.3 ± 0.6 measured for the CMF by Enoch et al. (2008). Further agreement with the CMF is seen in figure 10, which shows the cumulative mass function $N(> M) = \int_M^\infty n(M) dM$ for our data (black line) and the prestellar cores from Perseus, Ophiuchus and Serpens presented in Enoch et al. (2009) (grey line). Here we have scaled both populations to the Bonnor Ebert mass,

$$M_{BE} = \frac{1.18 c_s^4}{G^{3/2} \rho_0^{1/2}}.$$

The observed points used a Bonnor Ebert mass of $1.5 M_\odot$, which corresponds to a background density of $\approx 9000 \text{ cm}^{-3}$ at 10 K. This is somewhat higher than the mean density in these clouds, but not unreasonable for the ambient density immediately surrounding the cores, which have mean densities of $\approx 10^5 \text{ cm}^{-2}$. The simulated cores used the mean density in the box, which in the scaling used throughout this paper gives $M_{BE} = 10 M_\odot$, though strictly speaking this is a free value. The observational data are all prestellar cores from the 1.1 mm BoloCam survey of Perseus, Serpens and Ophiuchus presented in Enoch et al. (2006), Young et al. (2006), Enoch et al. (2007), respectively, that do not have an associated infrared source in the *Spitzer* c2d catalog. The majority of these objects can reasonably be assumed to be self gravitating, based on comparisons of the Perseus cores to kinematic information from the molecular line survey of the same region by Rosolowsky et al. (2008). As our simulation only attempts to model the prestellar core phase of star formation, and not the formation of the actual star itself, this sample of objects is the best observational counterpart for comparison.

8. CONCLUSIONS

In this work, we present density and magnetic field distributions for a super Alfvénic turbulence simulation with self gravity. The simulation was run with the AMR extension of Enzo described by Collins et al. (2010),

allowing us unprecedented spatial resolution. Super-Alfvénic turbulence has been proposed as the primary mechanism for star formation, providing good explanations of the star formation rate (Krumholz & McKee 2005; Padoan & Nordlund 2009) and initial mass function (Padoan & Nordlund 2002). Here we provide two checks of this model against observations, and explore deviations from the predictions of super-Alfvénic turbulence caused by the addition of self gravity.

We find in Sections 3 and 4 that power law tails develop for both high density and high magnetic field in volume and mass weighted PDFs, $P(\rho) \propto \rho^{-1.67}$ and $P(B) \propto B^{-2.74}$, respectively. The volume-weighted density PDF is consistent with the prediction of a singular isothermal sphere (SIS) (Kritsuk et al. 2010a) $P(\rho_{\text{SIS}}) \propto \rho^{-1.5}$.

The relationship between the magnetic field and the density also shows a power law behavior $B \propto \rho^{0.48}$ throughout the gas, consistent with the findings of Li et al. (2004), who found a similar behavior in the peak density/field relation in cores. This then allows us to explain the magnetic PDF, by combining this result with the density PDF.

Gravitationally bound cores found in our simulation were compared against several observational surveys. Comparisons with the most recent Zeeman splitting measurements of Troland & Crutcher (2008) and Falgarone et al. (2008) show that the mass-to-flux ratio in our simulations agrees in value and behavior with those found observationally. The relationship between field strength and column density is fit to a power law, $B \propto N^{0.57}$, demonstrating that significant mass-to-flux, thus magnetic support, is lost due to motion along the field lines.

Comparing our core mass function (CMF) to that of prestellar cores in Enoch et al. (2008), we again find excellent agreement. A slope of 2.1 ± 0.6 agrees with their fit value of 2.3 ± 0.6 , and cumulative mass distributions line up almost identically. The relatively good match between the observed CMF and the observed IMF indicates that the IMF is determined well before the onset of nuclear burning, at a relatively low (compared to the protostar) density. A multiplicative offset of $> 1/4$ is seen between the cores of Enoch et al. (2008) and the observed IMF, indicating that as much as 3/4 of the mass is lost in the final collapse phase. However, this is only an upper limit to the lost fraction, as the peak of the observed CMF is heavily influenced by its completeness limit. Bound cores in our simulation agree with the observed CMF extremely well, indicating that super-Alfvénic turbulence and gravity are primarily responsible for the structure of the mass distribution of the CMF, and ultimately the IMF.

The authors would like to thank A. Kritsuk for his input and many useful discussions. The authors would like to acknowledge financial support from NSF grants AST0808184 and AST0908740, and computational resources provided by the National Institute for Computational Sciences under LRAC allocation MCA98N020 and TRAC allocation TG-AST090110.

REFERENCES

- Balsara, D. S. 2001, *Journal of Computational Physics*, 174, 614

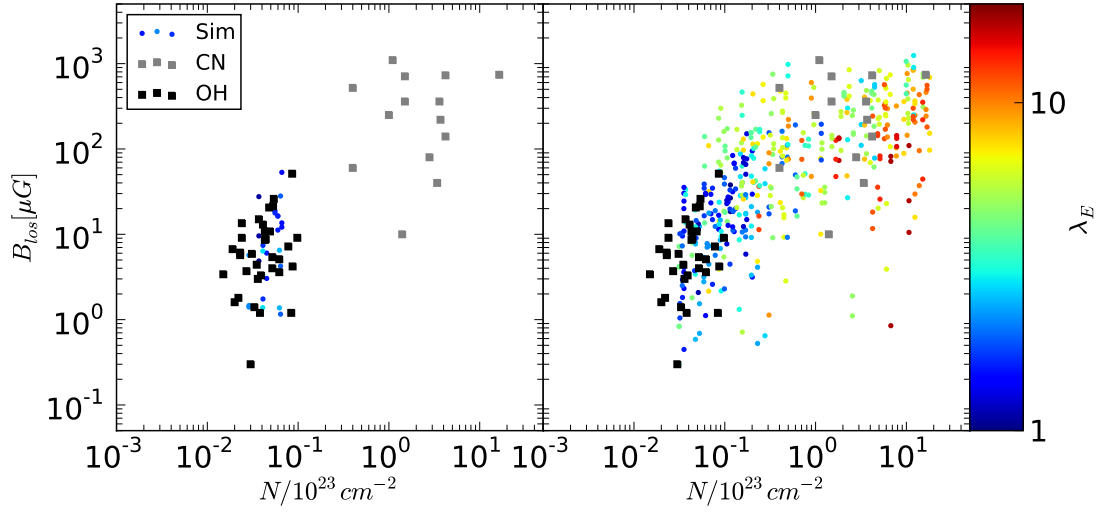


Figure 8. Line of sight magnetic field strength B_{los} vs column density N for three populations of cores: CN Zeeman splitting measurements of Falgarone et al. (2008) (grey squares); OH Zeeman splitting measurements of Troland & Crutcher (2008) (black squares); and bound objects in our simulation (colored points). Color indicates the ratio of gravitational to magnetic energy. At time $t = 0$ (left) and $t = 0.75 t_{ff}$ (right) Color indicates $\lambda_E = \sqrt{E_G/E_B}$

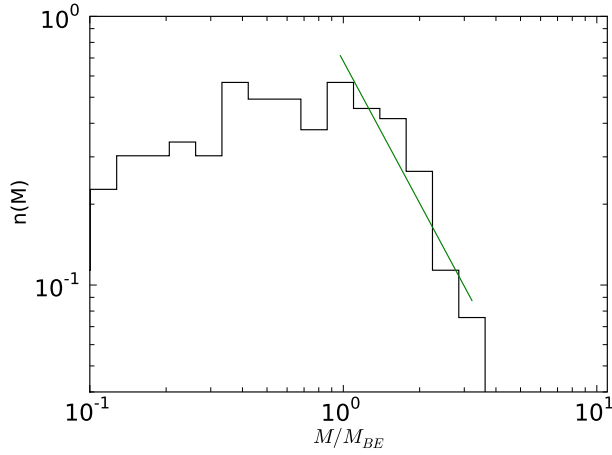


Figure 9. Mass distribution of bound cores. The fit line is $N(M) \propto M^{-2.1 \pm 0.6}$, consistent with both IMF and CMF measurements.

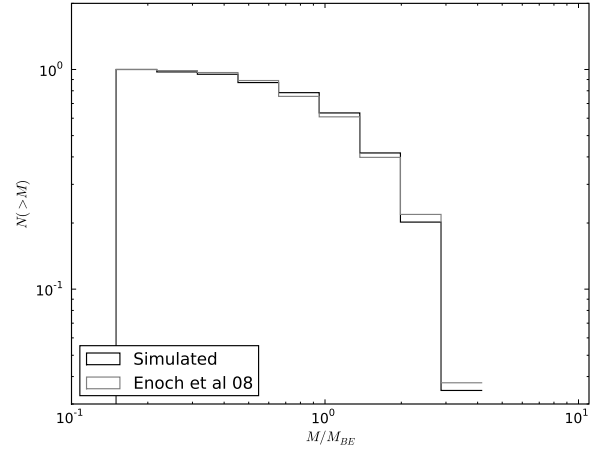


Figure 10. Cumulative mass distributions for our bound cores (black) and the prestellar cores from Enoch et al. (2008) (grey), relative to the Bonnor-Ebert mass. Here we have normalized the observed cores to $M_{BE} = 1.5 M_{\odot}$ for comparison

Beetz, C., Schwarz, C., Dreher, J., & Grauer, R. 2008, *Physics Letters A*, 372, 3037
 Bertoldi, F., & McKee, C. F. 1992, *ApJ*, 395, 140
 Bonnell, I. A., Bate, M. R., Clarke, C. J., & Pringle, J. E. 2001, *MNRAS*, 323, 785
 Bourke, T. L., Myers, P. C., Robinson, G., & Hyland, A. R. 2001, *ApJ*, 554, 916
 Collins, D. C., Xu, H., Norman, M. L., Li, H., & Li, S. 2010, *ApJS*, 186, 308
 Crutcher, R. M. 1999, *ApJ*, 520, 706
 Dib, S., Hennebelle, P., Pineda, J. E., Csengeri, T., Bontemps, S., Audit, E., & Goodman, A. A. 2010, *ArXiv e-prints astro-ph/1003.5118*
 Enoch, M. L., Evans, N. J., Sargent, A. I., & Glenn, J. 2009, *ApJ*, 692, 973
 Enoch, M. L., Evans, II, N. J., Sargent, A. I., Glenn, J., Rosolowsky, E., & Myers, P. 2008, *ApJ*, 684, 1240

Enoch, M. L., Glenn, J., Evans, II, N. J., Sargent, A. I., Young, K. E., & Huard, T. L. 2007, *ApJ*, 666, 982
 Enoch, M. L., et al. 2006, *ApJ*, 638, 293
 Falgarone, E., Troland, T. H., Crutcher, R. M., & Paubert, G. 2008, *A&A*, 487, 247
 Federrath, C., Glover, S. C. O., Klessen, R. S., & Schmidt, W. 2008a, *Physica Scripta Volume T*, 132, 014025
 Federrath, C., Klessen, R. S., & Schmidt, W. 2008b, *ApJ*, 688, L79
 Federrath, C., Roman-Duval, J., Klessen, R. S., Schmidt, W., & Mac Low, M. 2010, *A&A*, 512, A81+
 Fiedler, R. A., & Mouschovias, T. C. 1993, *ApJ*, 415, 680
 Fromang, S., Hennebelle, P., & Teyssier, R. 2006, *A&A*, 457, 371, *ramses*
 Gammie, C. F., Lin, Y., Stone, J. M., & Ostriker, E. C. 2003, *ApJ*, 592, 203

- Gardiner, T. A., & Stone, J. M. 2005, *Journal of Computational Physics*, 205, 509
- Heitsch, F., Mac Low, M., & Klessen, R. S. 2001, *ApJ*, 547, 280
- Kainulainen, J., Beuther, H., Henning, T., & Plume, R. 2009, *A&A*, 508, L35
- Klessen, R. S. 2000, *ApJ*, 535, 869
- Kritsuk, A. G., Norman, M. L., Padoan, P., & Wagner, R. 2007, *ApJ*, 665, 416
- Kritsuk, A. G., Norman, M. L., & Wagner, R. 2010a, *ArXiv e-prints astro-ph:1007.2950*
- Kritsuk, A. G., Ustyugov, S. D., Norman, M. L., & Padoan, P. 2009, in *ASP Conf. Ser.*, Vol. 406, *Numerical Modeling of Space Plasma Flows: ASTRONUM-2008*, ed. N. V. Pogorelov, E. Audit, P. Colella, & G. P. Zank (San Fransisco: ASP), 15
- Kritsuk, A. G., Ustyugov, S. D., Norman, M. L., & Padoan, P. 2010b, in *ASP Conf. Ser.*, Vol. 429, *Numerical Modeling of Space Plasma Flows: ASTRONUM-2009*, ed. N. V. Pogorelov (San Fransisco: ASP), 15
- Krumholz, M. R., & McKee, C. F. 2005, *ApJ*, 630, 250
- Lemaster, M. N., & Stone, J. M. 2008, *ApJ*, 682, L97
- Li, P. S., Norman, M. L., Mac Low, M.-M., & Heitsch, F. 2004, *ApJ*, 605, 800
- Li, S., Li, H., & Cen, R. 2008, *ApJS*, 174, 1
- Lunttila, T., Padoan, P., Juvela, M., & Nordlund, Å. 2008, *ApJ*, 686, L91
- Mac Low, M.-M. 1999, *ApJ*, 524, 169
- Motte, F., Andre, P., & Neri, R. 1998, *A&A*, 336, 150
- Mouschovias, T. C. 1987a, in *NATO ASIC Proc. 210: Physical Processes in Interstellar Clouds*, ed. G. E. Morfill & M. Scholer, 453
- Mouschovias, T. C. 1987b, in *NATO ASIC Proc. 210: Physical Processes in Interstellar Clouds*, ed. G. E. Morfill & M. Scholer, 491–552
- Myers, P. C. 2010, *ApJ*, 714, 1280
- Nakano, T., & Nakamura, T. 1978, *PASJ*, 30, 671
- Nordlund, Å. K., & Padoan, P. 1999, in *Interstellar Turbulence*, ed. J. Franco & A. Carraminana, 218
- Padoan, P., Jones, B. J. T., & Nordlund, A. P. 1997a, *ApJ*, 474, 730
- Padoan, P., & Nordlund, Å. 1999, *ApJ*, 526, 279
- . 2002, *ApJ*, 576, 870
- . 2004, *ApJ*, 617, 559
- Padoan, P., & Nordlund, A. 2009, *ArXiv e-prints*
- Padoan, P., Nordlund, A., & Jones, B. J. T. 1997b, *MNRAS*, 288, 145
- Padoan, P., Nordlund, Å., Kritsuk, A. G., Norman, M. L., & Li, P. S. 2007, *ApJ*, 661, 972
- Passot, T., & Vázquez-Semadeni, E. 1998, *Phys. Rev. E*, 58, 4501
- Price, D. J., & Bate, M. R. 2008, *MNRAS*, 385, 1820
- Price, D. J., & Bate, M. R. 2010, in *American Institute of Physics Conference Series*, Vol. 1242, *American Institute of Physics Conference Series*, ed. G. Bertin, F. de Luca, G. Lodato, R. Pozzoli, & M. Romé, 205–218
- Price, D. J., & Monaghan, J. J. 2004, *MNRAS*, 348, 123
- Rosolowsky, E. W., Pineda, J. E., Foster, J. B., Borkin, M. A., Kauffmann, J., Caselli, P., Myers, P. C., & Goodman, A. A. 2008, *ApJS*, 175, 509
- Salpeter, E. E. 1955, *ApJ*, 121, 161
- Scalo, J. 2005, in *Astrophysics and Space Science Library*, Vol. 327, *The Initial Mass Function 50 Years Later*, ed. E. Corbelli, F. Palla, & H. Zinnecker, 23
- Scalo, J., Vázquez-Semadeni, E., Chappell, D., & Passot, T. 1998, *ApJ*, 504, 835
- Schmidt, W., Kern, S. A. W., Federrath, C., & Klessen, R. S. 2010, *A&A*, 516, A25+
- Shu, F. H., Adams, F. C., & Lizano, S. 1987, *ARA&A*, 25, 23
- Slyz, A. D., Devriendt, J. E. G., Bryan, G., & Silk, J. 2005, *MNRAS*, 356, 737
- Smith, B. D., Turk, M. J., Sigurdsson, S., O’Shea, B. W., & Norman, M. L. 2009, *ApJ*, 691, 441
- Troland, T. H., & Crutcher, R. M. 2008, *ApJ*, 680, 457
- Truelove, J. K., Klein, R. I., McKee, C. F., Holliman, II, J. H., Howell, L. H., & Greenough, J. A. 1997, *ApJ*, 489, L179+
- Turk, M. 2008, in *Proceedings of the 7th Python in Science Conference*, ed. G. Varoquaux, T. Vaught, & J. Millman, Pasadena, CA USA, 46
- Vázquez-Semadeni, E. 1994, *ApJ*, 423, 681
- Vázquez-Semadeni, E., González, R. F., Ballesteros-Paredes, J., Gazol, A., & Kim, J. 2008, *MNRAS*, 390, 769
- Vázquez-Semadeni, E., Kim, J., Shadmehri, M., & Ballesteros-Paredes, J. 2005, *ApJ*, 618, 344
- Young, K. E., et al. 2006, *ApJ*, 644, 326